

# A numerical-continuation-enhanced flexible boundary condition scheme applied to Mode I and Mode III fracture

Maciej Buze\*

*School of Mathematics, Cardiff University, Senghennydd Road, Cardiff, CF24 4AG, United Kingdom*

James R. Kermode†

*Warwick Centre for Predictive Modelling, School of Engineering,  
University of Warwick, Coventry CV4 7AL, United Kingdom*

(Dated: March 27, 2022)

Motivated by the inadequacy of conducting atomistic simulations of crack propagation using static boundary conditions that do not reflect the movement of the crack tip, we extend Sinclair’s flexible boundary condition algorithm [*Philos. Mag.* **31**, 647–671 (1975)], enabling full solution paths for cracks to be computed with pseudo-arclength continuation, and present a method for incorporating more detailed far-field information into the model for next to no additional computational cost. The new algorithms are ideally suited to study details of lattice trapping barriers to brittle fracture and can be easily incorporated into density functional theory and multiscale quantum/classical QM/MM calculations. We demonstrate our approach for Mode III fracture with a 2D toy model, and for Mode I fracture of silicon using realistic interatomic potentials, highlighting the superiority of the new approach over employing a corresponding static boundary condition. In particular, the inclusion of numerical continuation enables converged results to be obtained with realistic model systems containing a few thousand atoms, with very few iterations required to compute each new solution. We also introduce a method to estimate the lattice trapping range of admissible stress intensity factors  $K_- < K < K_+$  very cheaply and demonstrate its utility on both the toy and realistic model systems.

## I. INTRODUCTION

Atomistic modelling of brittle fracture in crystals goes back to the pioneering work carried out by Sinclair and coworkers in the 1970s [1–3]; for a recent review of contributions made to our understanding of fracture from atomistic simulations see Refs. 4 and 5. The principal distinction from continuum models is the discreteness of the atomic lattice, which leads to the concept of lattice trapping, first identified by Thomson in 1971 [6]. A consequence of lattice trapping is that cracks remain stable over a range of stress intensity factors  $K_- < K < K_+$ . Lattice trapping can lead to anisotropy in propagation directions [7], and the associated energy barriers imply that cleavage does not necessarily produce smooth fracture surfaces at low energies [8]. The phenomenon has a dynamical analogue, the velocity gap, which is a forbidden band of crack velocities at low temperatures [9]. The velocity gap vanishes at larger temperatures; thermal activation over lattice trapping barriers has been proposed as an explanation for observations of low speed crack propagation on the (110) cleavage plane in silicon [10].

Detailed investigation of these phenomena are currently extremely challenging for two interconnected reasons. Firstly, realistic interatomic potentials capable of describing the very high strains near crack tips are very hard to construct [11]. At the same time, the requirement for large model systems and the strong coupling between lengthscales associated with fracture make the application of quantum mechanical techniques such as density functional theory (DFT) extremely challeng-

ing, despite the considerable success such techniques have enjoyed elsewhere in materials science [12]. Even when accurate atomistic models are available, determining the relevant stable crack tip configurations and the energy pathways that link them is extremely challenging because of the high dimensionality of the atomistic configuration space [10]. The picture is further complicated if the modelled crack propagates, causing an effective shift of origin of the entire strain field, which is often not reflected in the supplied boundary condition.

In the mathematical sciences, numerical continuation techniques have been previously applied to study crack propagation in Refs. 13 and 14. Relatedly, a mathematically rigorous numerical analysis of domain size effects for a static boundary condition scheme coupled with numerical continuation techniques has been conducted in Ref. 15. It provides a basic framework in which proving convergence rates to the infinite limit is possible and is the principal motivation for the current work.

Here, we return to the flexible boundary condition (FBC) approach introduced by Sinclair [3]. In this class of approaches, a localised atomic core region is coupled to a linear elastic far-field. The method has been developed and applied extensively to model dislocations [16–18], but applications to fracture have received comparatively little attention. We augment the FBC method, and address the challenge of identifying and analysing stable and unstable crack tip configurations by combining it with numerical continuation techniques. We demonstrate our ideas firstly for Mode III fracture in a toy model of a 2D crystal, considered a useful stepping stone for our theory, as it has readily calculable exact Hessians and permits a mathematically rigorous analysis. This is then followed by the more realistic and much-studied example of Mode I fracture of silicon on the (111) cleavage plane, using bond order potentials that have been modified to extend the interac-

\* BuzeM@cardiff.ac.uk

† J.R.Kermode@warwick.ac.uk

tion range and introduce screening to provide a qualitatively correct description of bond-breaking processes [19].

## II. METHODOLOGY

### A. Discrete Kinematics

For the purpose of describing the method, we first consider a simplified system consisting of a two-dimensional infinite crystal of atoms forming a triangular lattice and interacting via a known interatomic potential with a finite interaction radius, with a crack forming along the horizontal axis and a crack tip located at  $(\alpha, 0) \in \mathbb{R}^2$ . The position of the  $i$ th atom is denoted by  $\mathbf{x}(i) = (x_1(i), x_2(i), x_3(i)) \in \mathbb{R}^3$ , which is always of the form

$$\mathbf{x}(i) = \hat{\mathbf{x}}(i) + Y(i), \quad (1)$$

where  $\hat{\mathbf{x}}(i)$  is the crystalline lattice position and  $Y(i) = (Y_1(i), Y_2(i), Y_3(i))$  is the displacement from the crystalline lattice.

The theory will be presented for two crack modes: pure Mode III, described by out-of-plane displacements ( $Y_1 = Y_2 = 0$ ), and Mode I, in which in-plane displacements dominate ( $Y_3 = 0$ ). Atoms are assumed to interact according to an interatomic potential  $\phi$ , which, to avoid unnecessary technicalities is initially taken to be a pair potential with total energy of the form

$$E = \sum_{i \neq j} \phi(r_{ij}), \text{ where } r_{ij} = |\mathbf{x}(i) - \mathbf{x}(j)|. \quad (2)$$

The restriction to pair potentials is not needed for the analysis, and will be lifted in the numerical examples considered in Section III B.

Following the ideas of Sinclair [3], the system is divided into three regions. Region I, also known as *the defect core* is a finite collection of atoms, labelled from  $i = 1$  to  $i = N_1$ , in the vicinity of the crack tip. Each atom in Region I is free to move, thus, in Mode I, there are  $2N_1$  degrees of freedom associated with Region I and, in Mode III, there are  $N_1$  degrees of freedom.

Atoms in Region II, known as *the interface*, all contain at least one atom from Region I in its interaction range and are labelled from  $i = N_1 + 1$  to  $i = N_2$ . Region III is *the far field*.

The total energy is divided into two parts

$$E = E^{(1)}(\{\mathbf{x}(i)\}_{i=1}^{N_2}) + E^{(2)}(\{\mathbf{x}(i)\}_{i>N_1}). \quad (3)$$

The far-field part represented by  $E^{(2)}$  is known to be unbounded for a body containing a crack opening. In practical applications the quantity of interest is thus the energy difference between a suitably chosen initial configuration  $\{\mathbf{x}_0(i)\}$  and a relaxed configuration  $\{\mathbf{x}(i)\}$ , which is denoted by

$$E - E_0 = E(\{\mathbf{x}(i)\}) - E(\{\mathbf{x}_0(i)\}).$$

There are different ways of specifying the behaviour of atoms in Region II and III. In what follows we first review

two approaches, namely a simple static boundary condition specified by continuum linearised elasticity and a simplified version of the flexible boundary scheme due to Sinclair [3].

Subsequently, we show how the flexible boundary scheme leads to a simple equation to check for admissible values of the stress intensity factor for which equilibria exist, which motivates defining an alternative version of the flexible boundary scheme with improved accuracy.

This is then followed by a discussion about applying numerical continuation techniques to both formulations and the resulting bifurcation diagrams capturing crack propagation, energy barriers and the phenomenon of lattice trapping [6].

### B. Static boundary scheme

Prescribing a simple static far-field boundary condition consists of constraining atoms in both Region II and Region III to be displaced according to continuum linear elasticity (CLE) equations arising from the mode of crack considered, the Cauchy-Born relation and the interatomic potential employed. Crucially, these equations are derived for the crack tip fixed at the origin, i.e. with  $\alpha = 0$  and remain unchanged even if a relaxation of the core region yields a different crack tip position.

In both idealised modes of crack considered, it can be shown that the atomistic model posed on a triangular lattice gives rise to an isotropic CLE equation [20]. In particular, with the crack tip assumed to coincide with the origin of the coordinate system and polar coordinates  $\hat{\mathbf{x}}(i) = r_i(\cos \theta_i, \theta_i)$  employed, the anti-plane CLE displacement for Mode III crack is given by

$$U_{\text{CLE}}^{\text{III}}(i) = \sqrt{r_i}(0, 0, \sin(\theta_i/2)), \quad (4)$$

whereas the isotropic in-plane CLE displacement for Mode I crack is given by

$$U_{\text{CLE}}^{\text{I}}(i) = \sqrt{r_i} \begin{pmatrix} 3 \cos(\theta_i/2) - \cos(3\theta_i/2), \\ 5 \sin(\theta_i/2) - \sin(3\theta_i/2), 0 \end{pmatrix}. \quad (5)$$

The anisotropic Mode I case will be considered in Section III B, where we also allow out-of-plane relaxation as well as in-plane. The superscript on  $U_{\text{CLE}}$  distinguishing different crack modes is dropped whenever a distinction is not needed. The displacement fields we consider are in fact of the form  $\{K U_{\text{CLE}}(i)\}$ , where  $K \in \mathbb{R}$  is the stress intensity factor.

A suitable way of encoding this far-field behaviour is to consider configurations  $\{\mathbf{x}(i)\}$  in the form

$$\mathbf{x}(i) = \hat{\mathbf{x}}(i) + K U_{\text{CLE}}(i) + U(i), \quad (6)$$

where, as in (1),  $\hat{\mathbf{x}}(i)$  is the crystalline lattice position and  $U(i)$  the atomistic correction of the  $i$ th atom, accounting for the fact that atoms within Region I are free to relax under the interatomic potential. This correction is constrained to satisfy  $U(i) = \mathbf{0}$  for  $i > N_1$ , which ensures that atoms outside the core remain fixed at the CLE displacement field.

In this framework the initial configuration  $\{\mathbf{x}_0(i)\}$  against which the energy difference is computed corresponds to setting  $U(i) = 0$  for all  $i$ . As a result, it trivially holds that

$$E_2(\{\mathbf{x}(i)\}_{i>N_1}) = E_2(\{\mathbf{x}_0(i)\}_{i>N_1}),$$

and hence

$$E - E_0 = E(\{\mathbf{x}(i)\}_{i=1}^{N_2}) - E(\{\mathbf{x}_0(i)\}_{i=1}^{N_2}),$$

which is a finite quantity.

If one defines a function of  $(\{U(i)\}, K)$  given by

$$\mathbf{F}_0 = (\{\mathbf{f}(i)\}_{i=1}^{N_1}), \quad (7)$$

where  $\mathbf{f}(i) = -\frac{\partial E}{\partial \mathbf{x}(i)}$  is the force acting on the  $i$ th atom, then an equilibrium configuration can be found by solving  $\mathbf{F}_0 = \mathbf{0}$ .

For a fixed  $K$ , in Mode III, this is a system of  $N_1$  equations for  $N_1$  variables, and, in Mode I there are  $2N_1$  equations for  $2N_1$  variables. In a fully 3D case, to be considered in numerical tests in Section III B, the system considered consists of  $3N_1$  equations for  $3N_1$  variables.

The remaining difficulty is the interplay between the choice of  $K$  and the crack tip position. This will be addressed in Section II D with the help of numerical continuation, in particular highlighting fundamental limitations of the static boundary scheme.

### C. Flexible boundary scheme

#### 1. Standard formulation

The central idea of the flexible boundary scheme described by Sinclair [3] is to allow the crack tip position  $(\alpha, 0)$  to vary. The displacements can be shifted to account for the current crack tip position by redefining the polar coordinates used in (4) and (5) so that

$$r_i(\cos \theta_i, \sin \theta_i) = \hat{\mathbf{x}}(i) - (\alpha, 0).$$

The configurations considered are, similarly to (6), of the form

$$\mathbf{x}(i) = \hat{\mathbf{x}}(i) + K U_{\text{CLE}}^\alpha(i) + U(i),$$

where the CLE displacement is now written as  $U_{\text{CLE}}^\alpha$  to emphasise the dependence on  $\alpha$  through the shift of the polar coordinate system. The chosen initial unrelaxed configuration  $\{\mathbf{x}_0(i)\}$  is obtained by setting  $\alpha = 0$  and  $U(i) = 0$  for all  $i$ .

The effect that varying  $\alpha$  has on the system can be captured by considering the notion of a *generalised force*

$$f_\alpha^\infty = -\frac{\partial E}{\partial \alpha} = \sum_i -\frac{\partial E}{\partial \mathbf{x}(i)} \cdot \frac{\partial \mathbf{x}(i)}{\partial \alpha} = \sum_i \mathbf{f}(i) \cdot K V_\alpha(i), \quad (8)$$

where  $V_\alpha = -\partial_1 U_{\text{CLE}}^\alpha$ . As stated, this is an infinite sum, which can be shown to be convergent since  $U_{\text{CLE}}$  solves the CLE equation [21].

Somewhat arbitrarily, Sinclair assumes that in Region III the crystal is fully 'linearly elastic' [3], in the sense that

the continuum CLE displacement is an equilibrium by itself, meaning that

$$\mathbf{f}(i) = 0, \text{ for } i > N_2, \quad (9)$$

for any choice of  $K$  and  $\alpha$ , effectively truncating the infinite sum in (8).

The Sinclair scheme can be formalised by defining a function of  $(\{U(i)\}, K, \alpha)$  given by

$$\mathbf{F}_1 = (\{\mathbf{f}(i)\}_{i=1}^{N_1}, f_\alpha), \quad (10)$$

where

$$f_\alpha = \sum_{i=1}^{N_2} \mathbf{f}(i) \cdot K V_\alpha(i). \quad (11)$$

An equilibrium configuration in this scheme is then obtained by solving  $\mathbf{F}_1 = \mathbf{0}$ .

Notably, the summation in (11) is effectively over  $\{i\}_{i=N_1+1}^{N_2}$ , since at an equilibrium  $\mathbf{f}(i) = 0$  for  $i \leq N_1$ .

Obviously, (9) is only true in an approximate sense, which leaves open to interpretation whether the truncation enforced through (9) is the optimal choice.

It is further worth noting that in the limit when  $N_1 \rightarrow \infty$ , the generalised force  $f_\alpha$  in (11) is null at any equilibrium, hence the extra equation  $f_\alpha = 0$  is effectively redundant, which strongly hints that the role of the flexible scheme lies in improving the convergence rate to the single infinite limit. A mathematically rigorous proof of this result will be a subject of further study.

To compute the energy difference  $E - E_0$  in the new scheme, we follow the procedure described in Ref. 3, Appendix 1, with the far-field contribution to the energy  $E^{(2)} - E_0^{(2)}$  from (3) approximated as

$$E^{(2)} - E_0^{(2)} = -\frac{1}{2} \sum_{i=N_1+1}^{N_2} \left( \mathbf{f}^{(2)}(i) + \mathbf{f}_0^{(2)}(i) \right) \cdot (\mathbf{x}(i) - \mathbf{x}_0(i)),$$

where  $\mathbf{f}^{(2)}(i) = -\frac{\partial E^{(2)}}{\partial \mathbf{x}(i)}$ .

Making sense of the arguably unsubstantiated far-field approximation in (9) as well as addressing the question of convergence leads to several interesting realisations that will be addressed in the next section.

#### 2. Predicting admissible stress intensity factors

The strain fields associated with atomistic corrections  $\{U(i)\}$  are known to decay more quickly away from the core than the strain fields associated to  $\{U_{\text{CLE}}(i)\}$  (proven rigorously in a simplified setup in Ref. 22), meaning that their contributions are effectively negligible beyond a small region around the crack tip. It can thus be conjectured that a reasonable approximation to the flexible boundary scheme condition  $f_\alpha = 0$ , defined in (11), is to allow the unrelaxed configuration

$\{\mathbf{x}_0(i)\}$  to depend on  $\alpha$  and look at the generalised force at the unrelaxed configuration, namely

$$-\frac{\partial E_0}{\partial \alpha} = \sum_i -\frac{\partial E_0}{\partial \mathbf{x}_0(i)} \cdot \frac{\partial \mathbf{x}_0(i)}{\partial \alpha} = \sum_i \mathbf{f}_0(i) \cdot K V_\alpha(i).$$

Employing the same truncation as in (9), we can postulate a condition  $f_\alpha^0 = 0$ , where

$$f_\alpha^0 = \sum_{i=1}^{N_2} \mathbf{f}_0(i) \cdot K V_\alpha(i). \quad (12)$$

With the unrelaxed configuration  $\{\mathbf{x}_0(i)\}$ , now determined solely by  $K$  and  $\alpha$ , verifying whether  $f_\alpha^0 = 0$  holds is numerically very straightforward.

It will be shown in Section III A 3 and Section III B that solving  $f_\alpha^0 = 0$  provides a good estimate for the admissible values of the stress intensity factor and that there in fact exists a continuous path of solutions with  $K$  values nearly perfectly oscillating around a fixed interval of admissible values  $K_- < K < K_+$ .

With the numerical tests indicating that the predicted interval is strongly dependent on the size of the computational domain, it seems plausible that changing the far-field truncation rule from (9) can have a drastic effect on the computed solution path. This will be investigated in the next section.

### 3. Effect of changing far-field truncation rule

The truncation in (9) is equivalent to stating that the atomistic information associated with atoms in Region III, which conceptually is an infinite far field, is completely disregarded. One can provide the flexible boundary scheme with more atomistic input from Region III by changing the truncation in (9) to

$$\mathbf{f}(i) = 0, \text{ for } i > N_3, \quad (13)$$

where  $N_3 > N_2$  is much larger, e.g.  $N_3 = 4N_2$ . As a result, a new condition is  $\tilde{f}_\alpha = 0$ , where

$$\tilde{f}_\alpha = \sum_{i=1}^{N_3} \mathbf{f}(i) \cdot K V_\alpha(i).$$

Thus, the new approach testing the effect of different truncation can be formalised by defining a function of  $(\{U(i)\}, K, \alpha)$  given by

$$\mathbf{F}_2 = (\{\mathbf{f}(i)\}_{i=1}^{N_1}, \tilde{f}_\alpha), \quad (14)$$

with an equilibrium configuration obtained by solving  $\mathbf{F}_2 = 0$ .

The difference between the new scheme  $\mathbf{F}_2 = 0$  and the standard  $\mathbf{F}_1 = 0$  from (10) is most pronounced by observing that at an equilibrium in the new scheme, the previously defined truncated generalised force  $f_\alpha$  from (11) satisfies

$$f_\alpha = \sum_{i=N_2+1}^{N_3} \mathbf{f}(i) \cdot K V_\alpha(i). \quad (15)$$

The right-hand side admits input only from atoms in Region III, whose displacements are determined solely by  $\alpha$  and  $K$ , since by design,  $U(i) = 0$  for  $i \geq N_1$ , which highlights the general rationale behind this formulation: the far-field region within the computational domain is vastly enlarged, but only two degrees of freedom remain attached to it, meaning that in practice there is virtually no additional computational cost, apart from the ability to compute the right-hand side of (15).

It will be shown through numerical tests presented in Section III A 4 that the new scheme results in much improved accuracy for small sizes of the core region, implying that in practice the new scheme is numerically preferable, enabling increased accuracy to be achieved with decreased numerical cost.

### D. Pseudo-arclength numerical continuation

The basic premise of numerical continuation applied to the problem at hand is as follows. Suppose we have identified some  $K_1$  for which some equilibrium configuration  $\mathbf{x}_1$  exists. Can we use this knowledge to quickly find another equilibrium for  $K_1 + \delta K$ , for some small  $\delta K$ ? Such an approach will work well if there exists a continuous path of solutions  $K \mapsto \{U(i)_K\}_{i=1}^{N_1}$  (and  $K \mapsto \alpha_K$  in the case of the flexible boundary scheme). Such a path can be shown to exist, courtesy of Implicit Function Theorem [23], in the neighbourhood of  $K_1$  if the associated Hessian operator is invertible at  $K_1$ .

A more sophisticated version, which is particularly useful for the problem at hand, is known as the pseudo-arclength continuation. It postulates that the quantities involved all are smooth functions of an arclength parameter  $s$ . The question thus changes to: given some triplet  $(K_{s_1}, \{U_{s_1}(i)\}, \alpha_{s_1})$  (in the case of static boundary  $\alpha \equiv 0$  throughout) which specifies an equilibrium configuration  $\{\mathbf{x}_{s_1}(i)\}$ , can we find a new triplet for  $s_2 := s_1 + \delta s$ , for some small  $\delta s$ , which gives us a new equilibrium  $\{\mathbf{x}_{s_2}(i)\}$ ? The key advantage of this approach is that it can handle index-1 saddle points, which makes it a useful tool for studying energy barriers and the phenomenon of lattice trapping.

Numerical continuation can be incorporated into the framework by including  $K$  as a variable in the systems of equations  $\mathbf{F}_j = 0$  for  $j = 0, 1, 2$  defined in (7), (10), (14).

The inclusion of  $K$  as a variable renders each system of equations  $\mathbf{F}_j = 0$  is under-determined. With the assumption of there existing a continuous path of solutions, the schematic plot presented in Figure 1 motivates imposing the equation  $f_K = 0$  to close the system, where

$$f_K = \sum_{i=1}^{N_1} (U_{s_2}(i) - U_{s_1}(i)) \cdot \dot{U}_{s_1}(i) + (\alpha_{s_2} - \alpha_{s_1}) \dot{\alpha}_{s_1} + (K_{s_2} - K_{s_1}) \dot{K}_{s_1} - \delta s. \quad (16)$$

Here  $(\dot{K}_{s_1}, \{\dot{U}_{s_1}(i)\}, \dot{\alpha}_{s_1})$  refer to derivatives with respect to  $s$  evaluated at  $s_1$ . Note that in the static boundary scheme we simply have  $\alpha_{s_i} = 0$ , and hence  $\dot{\alpha}_{s_i} = 0$ , for all  $i$ .

If there indeed exist a continuous path of solutions, it can be

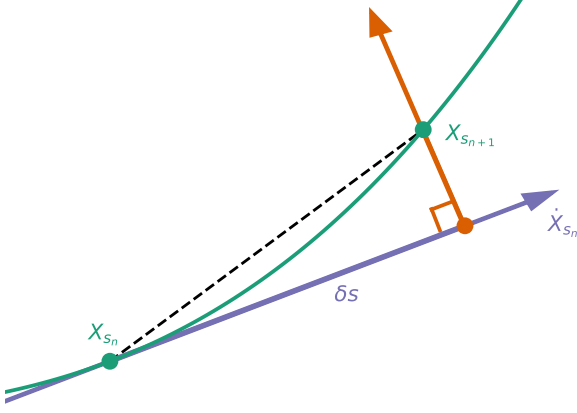


FIG. 1. Suppose  $X_{s_n} = (K_{s_n}, \{U_{s_n}(i)\}, \alpha_{s_n})$  belongs to the solution path, which is smooth (solid green line). The schematic two-dimensional plot indicates that imposing an extra constraint in the form of  $f_K = 0$  from (16) is equivalent to looking for solutions along the direction of the orange arrow, which is perpendicular to  $\dot{X}_{s_n}$ , represented by a purple arrow, with  $\delta s$  determining how far along  $\dot{X}_{s_n}$  we choose to travel. Choosing  $\delta s$  small enough ensures that the algorithm can safely traverse the solution path even along folds. It is further clear from the plot that, for  $\delta s$  sufficiently small,  $X_{s_n} + \delta s \dot{X}_{s_n}$  (orange dot) is a very good initial guess for subsequent steps of the Newton iteration.

shown [24] that for a step size  $\delta s$  small enough, a simple Newton iteration will converge to a new solution of  $(\mathbf{F}_j, f_K) = \mathbf{0}$ .

The remaining difficulty is to compute  $(\dot{K}_{s_1}, \{\dot{U}_{s_1}(i)\}, \dot{\alpha}_{s_1})$ . This can be achieved by first noting that with  $s$  being an arclength parameter, by definition it has to hold that

$$\sum_{i=1}^{N_1} \dot{U}_{s_1}(i) \cdot \dot{U}_{s_1}(i) + (\dot{K}_{s_1})^2 + (\dot{\alpha}_{s_1})^2 = 1. \quad (17)$$

This eliminates one degree of freedom. The remaining degrees of freedom can be eliminated by differentiating both sides of  $\mathbf{F}_j = 0$  with respect to arclength parameter  $s$ , which is possible under the assumption of there existing a smooth path of solutions. Details are presented in the Appendix.

The resulting pseudo-arclength continuation algorithms associated with both schemes are presented as Algorithm 1 and Algorithm 2.

---

#### Algorithm 1 Static boundary condition pseudo-arclength continuation

---

- 1: Given  $\delta s$ ;
  - 2: given a stable equilibrium configuration solving  $(\mathbf{F}_0, f_K) = \mathbf{0}$  determined by  $(K_{s_1}, \{U_{s_1}(i)\})$ ;
  - 3: compute  $(\dot{K}_{s_1}, \{\dot{U}_{s_1}(i)\})$  using (A.3);
  - 4: compute a new stable equilibrium configuration  $(K_{s_2}, \{U_{s_2}(i)\})$  by solving  $(\mathbf{F}_0, f_K) = \mathbf{0}$  using Newton iteration with initial guess  $(K_{s_1} + \delta s \dot{K}_{s_1}, \{U_{s_1}(i) + \delta s \dot{U}_{s_1}(i)\})$ ;
  - 5: **for**  $n > 1$  **do**
  - 6:   given  $(K_{s_n}, \{U_{s_n}(i)\})$  and  $(\dot{K}_{s_{n-1}}, \{\dot{U}_{s_{n-1}}(i)\})$ ;
  - 7:   compute  $(\dot{K}_{s_n}, \{\dot{U}_{s_n}(i)\})$  by solving linear system (A.6);
  - 8:   compute a new equilibrium configuration  $(K_{s_{n+1}}, \{U_{s_{n+1}}(i)\})$  by solving  $(\mathbf{F}_0, f_K) = \mathbf{0}$  using Newton iteration with initial guess  $(K_{s_n} + \delta s \dot{K}_{s_n}, \{U_{s_n}(i) + \delta s \dot{U}_{s_n}(i)\})$ ;
  - 9: **end for**
- 

---

#### Algorithm 2 Flexible boundary condition pseudo-arclength continuation

---

- 1: Given  $\delta s$ ;
  - 2: given a stable equilibrium configuration solving  $(\mathbf{F}_1, f_K) = \mathbf{0}$  determined by  $(K_{s_1}, \{U_{s_1}(i)\}, \alpha_{s_1})$ ;
  - 3: compute  $(\dot{K}_{s_1}, \{\dot{U}_{s_1}(i)\}, \dot{\alpha}_{s_1})$  using (A.5);
  - 4: compute a new stable equilibrium configuration  $(K_{s_2}, \{U_{s_2}(i)\}, \alpha_{s_2})$  by solving  $(\mathbf{F}_1, f_K) = \mathbf{0}$  using Newton iteration with initial guess  $(K_{s_1} + \delta s \dot{K}_{s_1}, \{U_{s_1}(i) + \delta s \dot{U}_{s_1}(i)\}, \alpha_{s_1} + \delta s \dot{\alpha}_{s_1})$ ;
  - 5: **for**  $n > 1$  **do**
  - 6:   given  $(K_{s_n}, \{U_{s_n}(i)\}, \alpha_{s_n})$  and  $(\dot{K}_{s_{n-1}}, \{\dot{U}_{s_{n-1}}(i)\}, \dot{\alpha}_{s_{n-1}})$ ;
  - 7:   compute  $(\dot{K}_{s_n}, \{\dot{U}_{s_n}(i)\}, \dot{\alpha}_{s_n})$  by solving linear system (A.7);
  - 8:   compute a new equilibrium configuration  $(K_{s_{n+1}}, \{U_{s_{n+1}}(i)\}, \alpha_{s_{n+1}})$  by solving  $(\mathbf{F}_1, f_K) = \mathbf{0}$  using Newton iteration with initial guess  $(K_{s_n} + \delta s \dot{K}_{s_n}, \{U_{s_n}(i) + \delta s \dot{U}_{s_n}(i)\}, \alpha_{s_n} + \delta s \dot{\alpha}_{s_n})$ ;
  - 9: **end for**
- 

Bearing in mind that most realistic interatomic potentials only provide analytic forces but not Hessians, meaning that Algorithm 2 cannot be readily used, as it requires a computation of the Hessian while differentiating  $\mathbf{F}_j = 0$  to get the tangent  $(\dot{K}_{s_n}, \{\dot{U}_{s_n}(i)\}, \dot{\alpha}_{s_n})$ , we also propose a simple finite-difference based approximate scheme as a Hessian-free alternative.

The method consists of first computing two stable equilibrium configurations determined by  $(K_{s_0}, \{U_{s_0}(i)\}, \alpha_{s_0})$  and  $(K_{s_1}, \{U_{s_1}(i)\}, \alpha_{s_1})$ , which crucially satisfy  $K_{s_1} \approx K_{s_0}$  (and also  $\alpha_{s_1} \approx \alpha_{s_0}$ ). In the first step the tangent  $(\dot{K}_{s_1}, \{\dot{U}_{s_1}(i)\}, \dot{\alpha}_{s_1})$  can be approximated as

$$\dot{U}_{s_1}(i) = \frac{1}{K_{s_1} - K_{s_0}} (U_{s_1}(i) - U_{s_0}(i)), \quad (18a)$$

$$\dot{\alpha}_{s_1} = \frac{1}{K_{s_1} - K_{s_0}} (\alpha_{s_1} - \alpha_{s_0}), \quad (18b)$$

$$\dot{K}_{s_1} = 1, \quad (18c)$$

with the last line a direct consequence of  $K$  being the effective continuation parameter in the first step, since it is  $K$  that is varied to obtain two stable equilibrium configurations.

With the tangents computed, one can now assemble the extended system and solve  $(\mathbf{F}_1, f_K) = \mathbf{0}$  to obtain an equilibrium

determined by  $(K_{s_2}, \{U_{s_2}(i)\}, \alpha_{s_2})$ . The switch to the extended system entails that now the arclength  $s$  is the continuation parameter and in particular  $s_2 - s_1 = \delta s$ , with  $\delta s$  fixed throughout. As a result, subsequent tangent approximations are computed, for  $n = 2, \dots$ , as

$$\dot{U}_{s_n}(i) = \frac{1}{\delta s} (U_{s_n}(i) - U_{s_{n-1}}(i)), \quad (19a)$$

$$\dot{\alpha}_{s_n} = \frac{1}{\delta s} (\alpha_{s_n} - \alpha_{s_{n-1}}), \quad (19b)$$

$$\dot{K}_{s_n} = \frac{1}{\delta s} (K_{s_n} - K_{s_{n-1}}). \quad (19c)$$

The details of this approximate scheme are summarised as Algorithm 3 below. In practical applications, to avoid possible numerical artefacts, the finite-difference approach could be substituted by the automatic differentiation approach [25].

---

**Algorithm 3** Hessian-free approximate flexible boundary condition pseudo-arclength continuation

---

- 1: Given  $\delta s$ ;
  - 2: given two stable equilibrium configurations solving  $(\mathbf{F}_1, f_K) = \mathbf{0}$ , determined by  $(K_{s_0}, \{U_{s_0}(i)\}, \alpha_{s_0})$  and  $(K_{s_1}, \{U_{s_1}(i)\}, \alpha_{s_1})$ , and satisfying  $K_{s_1} \approx K_{s_0}$  and  $\alpha_{s_1} \approx \alpha_{s_0}$ ;
  - 3: compute an approximate  $(\dot{K}_{s_1}, \{\dot{U}_{s_1}(i)\}, \dot{\alpha}_{s_1})$  using (18);
  - 4: compute a new stable equilibrium configuration  $(K_{s_2}, \{U_{s_2}(i)\}, \alpha_{s_2})$  by solving  $(\mathbf{F}_1, f_K) = \mathbf{0}$  using Newton iteration with initial guess  $(K_{s_1} + \delta s \dot{K}_{s_1}, \{U_{s_1}(i) + \delta s \dot{U}_{s_1}(i)\}, \alpha_{s_1} + \delta s \dot{\alpha}_{s_1})$ ;
  - 5: **for**  $n > 1$  **do**
  - 6:   given  $(K_{s_n}, \{U_{s_n}(i)\}, \alpha_{s_n})$  and  $(K_{s_{n-1}}, \{U_{s_{n-1}}(i)\}, \alpha_{s_{n-1}})$ ;
  - 7:   compute an approximate  $(\dot{K}_{s_n}, \{\dot{U}_{s_n}(i)\}, \dot{\alpha}_{s_n})$  using (19);
  - 8:   compute a new equilibrium configuration  $(K_{s_{n+1}}, \{U_{s_{n+1}}(i)\}, \alpha_{s_{n+1}})$  by solving  $(\mathbf{F}_1, f_K) = \mathbf{0}$  using Newton iteration with initial guess  $(K_{s_n} + \delta s \dot{K}_{s_n}, \{U_{s_n}(i) + \delta s \dot{U}_{s_n}(i)\}, \alpha_{s_n} + \delta s \dot{\alpha}_{s_n})$ .
  - 9: **end for**
- 

### III. RESULTS

In this section we discuss numerical tests based around applying the pseudo-arclength continuation to both the static and flexible boundary schemes.

We begin by directly comparing the static boundary scheme and the flexible boundary scheme when applied to a simple toy model, highlighting the superiority of the latter. This is then followed by a study of fracture on the (111) cleavage plane in silicon with two interatomic potentials.

#### A. Mode III toy model

We first consider a toy model of anti-plane Mode III fracture posed on a triangular lattice with lattice constant equal to unity and atoms interacting according to a nearest neighbour pair potential. The total energy is thus of the form

$$E = \sum_{\substack{i \neq j \\ |\hat{\mathbf{x}}(i) - \hat{\mathbf{x}}(j)| = 1}} \phi(r_{ij}), \quad \text{where } r_{ij} = |x_3(i) - x_3(j)|,$$

Quantity	Value
$a$	1.0
$\mu$	3.464
$\gamma$	0.333
$K_G$	0.49501

TABLE I. Values of the lattice constant  $a$ , shear modulus  $\mu$ , surface energy  $\gamma$  and Griffith stress intensity factor  $K_G$  computed for the Mode III toy model.

where

$$\phi(r) = \frac{1}{6} (1 - \exp(-3r^2)).$$

The resulting material properties are reported in Table I, including the shear modulus, the surface energy and the Griffith prediction for the critical stress intensity factor  $K_G$ .

To investigate domain size effects, we consider computational domains of different sizes, each geometrically represented by ball of radius  $R$  around the origin. The three choice of radii are (1)  $R = 32$ , (2)  $R = 64$  and (3)  $R = 128$ . The fully atomistic Region I is chosen to consists of all atoms with

$$|\hat{\mathbf{x}}(i)| < R - R_{\text{out}} - R_\phi, \quad (20)$$

where  $R_{\text{out}} = 2.1$  corresponds to the width of the annulus of atoms in the far field (Region III), and  $R_\phi = 1.1$  corresponds to the interaction radius, specifying the width of the annulus of atoms in the interfacial Region II. As a result in each scheme (1)  $N_1 = 3003$ , (2)  $N_1 = 13402$  and (3)  $N_1 = 56500$ , respectively.

#### 1. Pseudo-arclength continuation with static boundary scheme

Algorithm 1 is first employed to compute solution paths presented in Figure 2. With no knowledge of the actual crack tip position, the  $y$ -axis was chosen to represent the Euclidean norm of  $\{U_s(i)\}$ .

The plot confirms the intuitively clear notion that  $|U_s|$  will be smallest when there is no mismatch between the predicted crack tip position (in the static boundary scheme fixed at  $\alpha = 0$ ) and the actual crack tip position. Periodic wiggles further indicate a repeating bond-breaking behaviour.

The solution paths are heavily tilted, with no clear range of stress intensity factors for which equilibria exist, as  $K$  grows to effectively compensate for  $\alpha$  being fixed. In particular, no unstable equilibria are found and the energy is monotonically increasing in  $K$ , implying that no study of energy barriers is possible.

An ad-hoc post-processing way of estimating actual values of  $\alpha$  and  $K$  is to find

$$\min_{\alpha, K} \left( \sum_{i=1}^{N_*} |K_s U_{\text{CLE}}(i) + U_s(i) - K U_{\text{CLE}}^\alpha(i)|^2 \right), \quad (21)$$

where, in order to avoid boundary effects,  $\{i\}_{i=1}^{N_*}$  corresponds to all atoms such that  $|\hat{\mathbf{x}}(i)| < \frac{3}{4}R$ . The resulting plots of  $\alpha$  against  $K$  are shown with dashed lines in Figure 3.

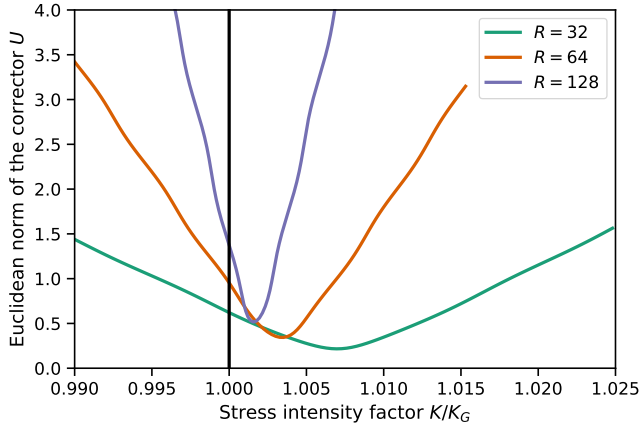


FIG. 2. Solution paths obtained for Mode III toy model using Algorithm 1 for three choices of domain size.

## 2. Pseudo-arclength continuation with flexible boundary scheme

Algorithm 2 is now employed to compute solution paths of the toy model for three different domain sizes, as described in Section III A.

A direct comparison of both scheme is shown in Figure 3, revealing that the flexible scheme is superior to the post-processing of the static scheme in terms of predicting the range of the stress intensity factors for which equilibria exist. In particular, the flexible scheme employed on a core region with radius  $R = 32$  is as accurate as the post-processed static scheme employed on a core region with radius  $R = 128$ .

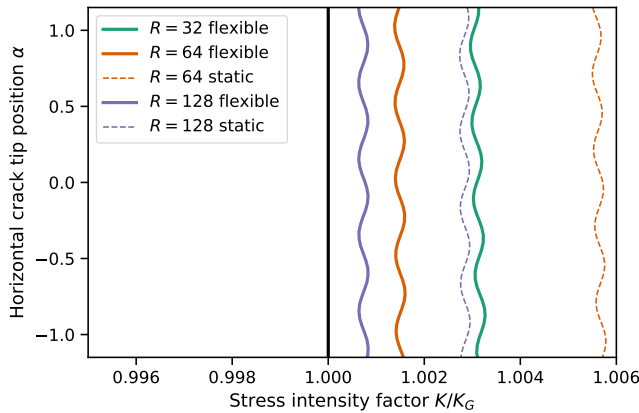


FIG. 3. Comparison of solutions paths obtained for Mode III toy model using Algorithm 2 (solid lines) and Algorithm 1 (dotted lines, post-processed via (21)) for three domain sizes (static  $R = 32$  case too far away to the right to include).

With unstable equilibrium configurations corresponding to index-1 saddle points captured in the flexible boundary scheme, a study of energy barriers is now feasible, as shown in Figure 4 and later in Figure 6.

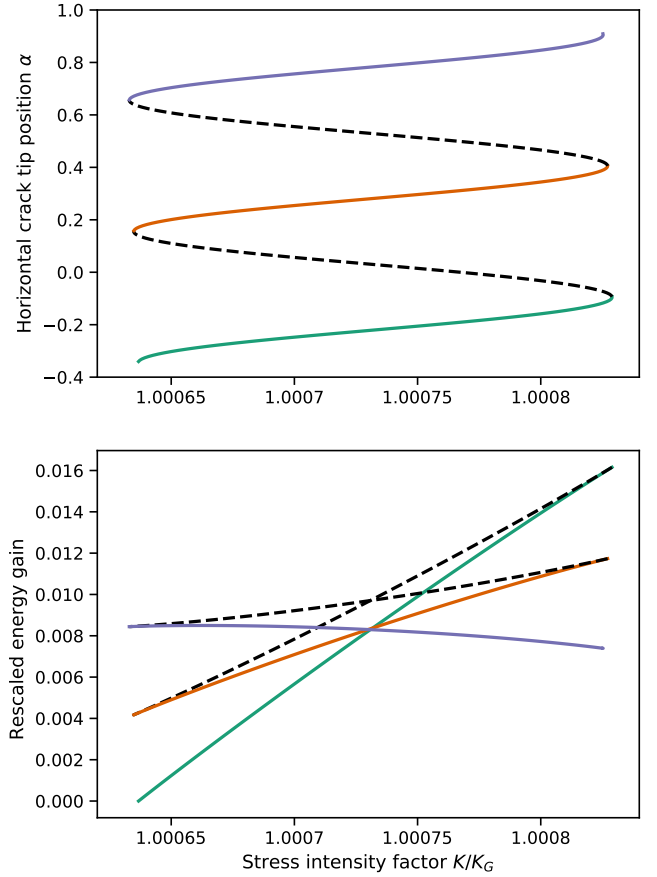


FIG. 4. A study of energy barriers in the Mode III toy model for computational domain of radius  $R = 128$ . The rescaled energy gain is  $(E - E_*)/E_*$ , where  $E_*$  is the energy of the bottom left configuration. The dashed parts of the solution path denote index-1 saddle points, which correspond to energetic cost of crack propagation at a given value of  $K$ , which can be seen by observing in the lower plot that dashed lines lie above their neighbouring solid lines. A nudged elastic band calculation further confirming this being the case is presented in Figure 6. The point where stable parts of the solution paths cross corresponds to the critical stress intensity factor  $K_c$ , notably not quite matching the Griffith stress intensity factor  $K_G$ . This phenomenon is elaborated upon in Section III A 5.

## 3. Predicting the admissible range for $K$

The ideas developed in Section II C 2 are now checked numerically for the toy model presented in Section III A, again employing three domain sizes. The results are presented in Figure 5.

The prediction of the range of admissible values of the stress intensity factor based on the CLE displacements only is shown to be fairly accurate, with the magnitude for  $K$  matching, while the predicted length of the interval considerably larger than in reality. Importantly, the prediction correctly shifts with the changing domain size, indicating that the range of admissible values for  $K$  is to a considerable extent determined by the far-field behaviour only, thus strongly motivating the new formulation of the flexible scheme presented in

Section II C 3, which will be tested numerically in the next section.

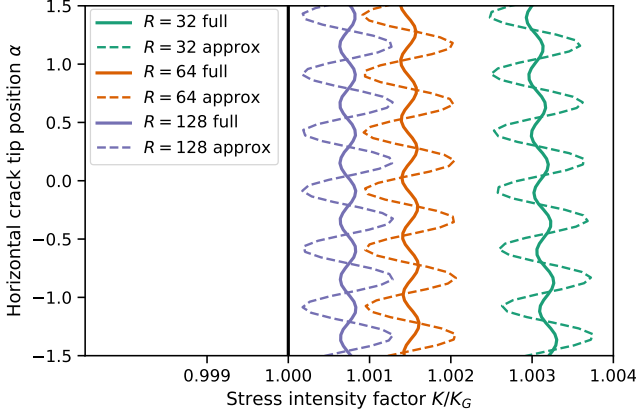


FIG. 5. Solutions paths computed for the Mode III toy model with Algorithm 2 (solid lines) for the three domain sizes, plotted against a corresponding path of approximate solutions obtained by solving  $f_\alpha^0 = 0$  from (12) (dashed lines).

#### 4. Pseudo-arclength continuation with flexible boundary scheme with extended far-field region

To test the effect of extending the far-field region discussed in Section II C 3, we consider a computational domain in the form of a ball of radius  $\bar{R} = 128$  with varying sizes of Region I.

As before, the core region is chosen to consists of all atoms satisfying (20), this time with (1)  $R = 8$ , (2)  $R = 16$ , (3)  $R = 32$  and (4)  $R = 64$ . Region II is again an annulus of width  $R_\phi = 1.1$  around Region I. Highlighting the key conceptual change, the width of the outer annulus corresponding to Region III is now  $\bar{R} - R + R_{\text{out}}$ , as opposed to just  $R_{\text{out}} = 2.1$  in the standard formulation. As a result  $N_3 = 58407$  and in each scheme (1)  $N_1 = 292$  (2)  $N_1 = 1046$ , (3)  $N_1 = 3946$  and (4)  $N_1 = 15323$ .

A suitably adjusted Algorithm 2 is now employed to compute solutions paths. The resulting plots of  $K$  against  $\alpha$  are presented in the middle panel of Figure 7, which also include the solution path computed with the standard flexible scheme with  $R = 256$  for comparison.

The extension of the far-field region drastically increases the accuracy of the flexible boundary scheme, with a tiny fully atomistic region required to have a very accurate prediction for the admissible range of values for the stress intensity factor. This is demonstrated quantitatively in the error analysis in Section III A 5.

Despite the large far-field region, the system of nonlinear equations associated with the new scheme when  $R = 8$  consists of merely 294 equations, as compared to the standard scheme when  $R = 128$ , which consists of 56502 equations, thus rendering the new scheme vastly superior.

Finally, to further confirm that the unstable solutions computed are indeed saddles and that no other critical points can

be found along the way, a modified version of the nudged elastic band method [26] has been employed on the domain with  $R = 32$ , with details presented in Figure 6.

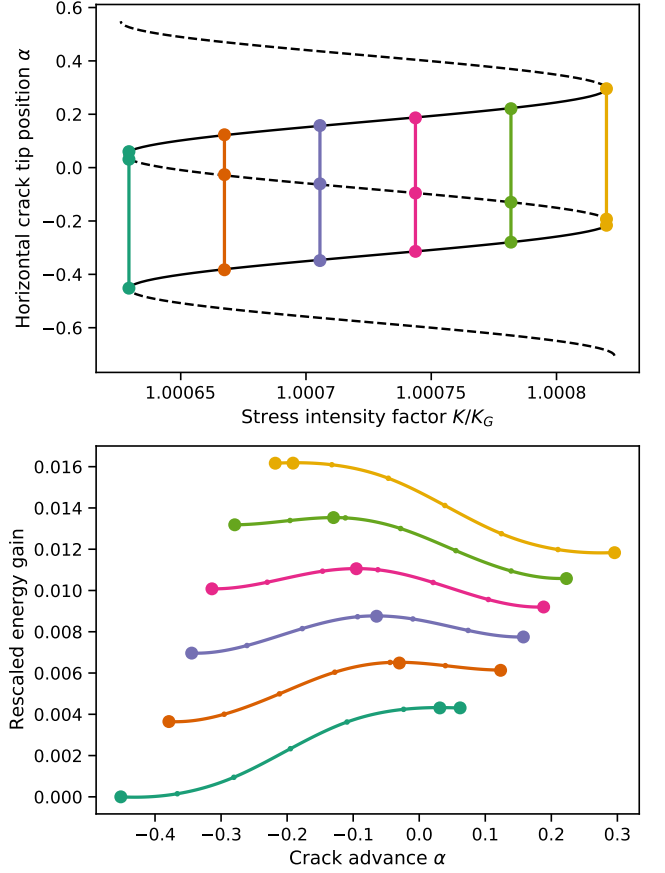


FIG. 6. A study of energy barriers in the flexible boundary scheme with extended far-field with  $R = 32$  and  $\bar{R} = 128$ . The top plot depicts the solution path in black. Six values of  $K$  are chosen and in each case an initial minimum energy path (MEP) is formed by linear interpolation between the first stable equilibrium, the saddle in between and the second stable equilibrium. The path is then optimised using the nudged elastic band method [26]. The resulting MEPs are shown in the bottom figure, together with larger dots representing the equilibria computed with pseudo-arclength continuation, thus confirming that the middle equilibrium is indeed a saddle and also confirming lack of other critical points along a given path.

#### 5. Error analysis

To conclude the numerical investigation of the toy model, a brief error analysis is presented in Figure 7. The reference solution path, imitating the infinite limit  $N_1 \rightarrow \infty$  is obtained with the standard flexible boundary scheme, as described in Section III A, with  $R = 256$ . Subsequently solution paths obtained with the standard flexible scheme with  $R = 8, 16, 32, 64$  are computed, as well as solution paths obtained with the extended flexible boundary scheme, as discussed in Section III A 4, with  $\bar{R} = 128$  and  $R = 8, 16, 32, 64$ .



The right-hand side plot in Figure 7 is produced by computing the Hausdorff distance [27] (intuitively the greatest of all the distances from a point on one line to the closest point on the other line) between a solution path of a given radius and the reference solution path.

Two things are apparent: firstly, the standard flexible scheme yields a rate of convergence of order  $O(R^{-1})$ , which improves upon a known rate of convergence  $O(R^{-1/2})$  of the static scheme proven in Ref. 15. A mathematically rigorous proof of the improved rate of convergence will be a subject of further study. Notably, the error analysis together with the study of energy barriers presented in Figure 4 and 6 clearly show that the Griffith prediction for the critical stress intensity factor  $K_G$  is only valid in the limit  $N_1 \rightarrow \infty$ .

Secondly, the extended far field flexible boundary scheme remains as accurate as the outer radius, which in the current study is fixed at  $\bar{R} = 128$ . The difference in accuracy is thus most apparent for small values of  $R$ , confirming the intuition behind this reformulation of the flexible boundary scheme. The underlying reasons for this are also to be explored in a future work.

### B. Mode I fracture of silicon on the (111) cleavage plane

We next test our new algorithms on a more complex problem: fracture of silicon on the (111) cleavage plane in the  $[11\bar{2}]$  propagation direction. This is known to be the preferred low-energy cleavage orientation, but the precise details of the lattice trapping barriers to brittle fracture remain elusive for the reasons outlined in the introduction, making this a problem of scientific interest as well as an interesting test case.

We consider two interatomic potentials known to give a qualitatively correct description of brittle fracture for this system: modifications of the Tersoff [28] and Kumagai [29] potentials, with the interaction length increased and additional screening functions introduced to improve the description of bond-breaking processes [19]. Without these modifications, neither potential predicts brittle behaviour. The modified potentials have been shown to predict lattice trapping ranges  $K_- < K < K_+$  for the (110) cleavage plane in reasonable agreement with DFT, albeit restricted to a small model system with static boundary conditions [19], and we thus use them here as a proxy for a fully description of interatomic bonding in silicon. The potentials have not previously been applied to study fracture on the (111) plane, in part because of the complexities introduced by the played by surface reconstructions such as the Pandey  $2 \times 1$   $\pi$ -bonded chain [12, 30], which we do not study here.

A number of small modifications to the FBC method described above are needed. Since analytical Hessians are not readily available for these potentials, we use the finite-difference reformulation of the scheme outlined in Algorithm 3. For comparison with the static case, we also consider a Hessian-free version of Algorithm 1, which can be obtained from Algorithm 3 by fixing  $\alpha = 0$  and  $\dot{\alpha} = 0$  throughout. The linear elastic predictor  $U_{\text{CLE}}^\alpha$  and its derivative  $V_\alpha$  are also redefined to account for the anisotropy of the silicon crys-

Quantity	Tersoff+S	Kumagai+S
$r_c / \text{\AA}$	6.0	6.0
$a / \text{\AA}$	5.432	5.429
$C_{11} / \text{GPa}$	143	165
$C_{12} / \text{GPa}$	75	65
$C_{44} / \text{GPa}$	69	77
$\gamma_{(111)} / \text{Jm}^{-2}$	1.20	0.89
$K_G / \text{MPa}\sqrt{\text{m}}$	1.07	0.97

TABLE II. Values of the cutoff radius  $r_c$ , lattice constant  $a$ , cubic elastic constants  $C_{11}$ ,  $C_{12}$ ,  $C_{44}$ , surface energy  $\gamma_{(111)}$  and Griffith stress intensity factor  $K_G$  computed with the screened versions of the Tersoff and Kumagai interatomic potentials.

tal using the near field solution for a crack in a rectilinear anisotropic elastic medium (noting that  $V_\alpha$  can conveniently be obtained from the  $xx$  and  $xy$  elements of the deformation tensor) [31]. The CLE solutions are expanded from two to three dimensions using plane strain loading conditions appropriate for a simulation cell periodic along the crack front line, i.e.  $Y_3 = 0$ , with the atomistic corrector  $U(i)$  for each atom also becoming three dimensional. In place of the Newton iteration, we solve  $(\mathbf{F}_1, f_K) = 0$  with a Newton-Krylov solver as implemented in the LGMRES package [32].

For large systems, it is necessary to precondition the solver. We used a general purpose preconditioner for materials systems [33], augmented by a diagonal rescaling of the  $f_\alpha$  and  $f_K$  components of the preconditioner to balance their magnitudes with that of the atomic forces  $\mathbf{f}(i)$  (as suggested by Sinclair [3]). Finally, the crack tip force  $f_\alpha$  is now computed by summing only over atoms in region II (or regions II and III for the extended far-field variant); as discussed after (11) this does not affect the equilibria obtained. A software implementation of the algorithm is available with the framework of the Atomic Simulation Environment (ASE) [34] as part of the open source matscipy package [35].

To setup the simulations, the lattice and elastic constants and the surface energy of the (111) plane are computed for each potential and are reported in Table II, along with the Griffith prediction for the critical stress intensity factor  $K_G$ , obtained using the relaxed surface energy  $\gamma_{(111)}$ .

Similar to the toy model above, we consider three domain radii (1)  $R = 32 \text{ \AA}$ , (2)  $R = 64 \text{ \AA}$  and (3)  $R = 128 \text{ \AA}$ , with the radius of the fully atomistic region I chosen to consider atoms with crystal positions

$$|\hat{x}(i)| < R - R_{\text{out}} - R_\phi$$

where now we take  $R_{\text{out}} = 2r_c = 12 \text{ \AA}$  as the width of the annulus of atoms defining Region III and  $R_\phi = r_c = 6.0 \text{ \AA}$  for the width of annulus of atoms in the interfacial Region II. For the extended far-field scheme, a further outer annular region of width  $r_c$  is added to ensure the forces on atoms in Region III are unaffected by the presence of the outer surface. The corresponding numbers of atoms in region I are (1)  $N_1 = 119$ , (2)  $N_1 = 1273$ , (3)  $N_1 = 7286$ , respectively. Since we now work in 3D, there are  $3N_1 + 1$  degrees of freedom for the Newton-Krylov solver for the static arc-length calculation, and  $3N_1 + 2$  for the flexible case.

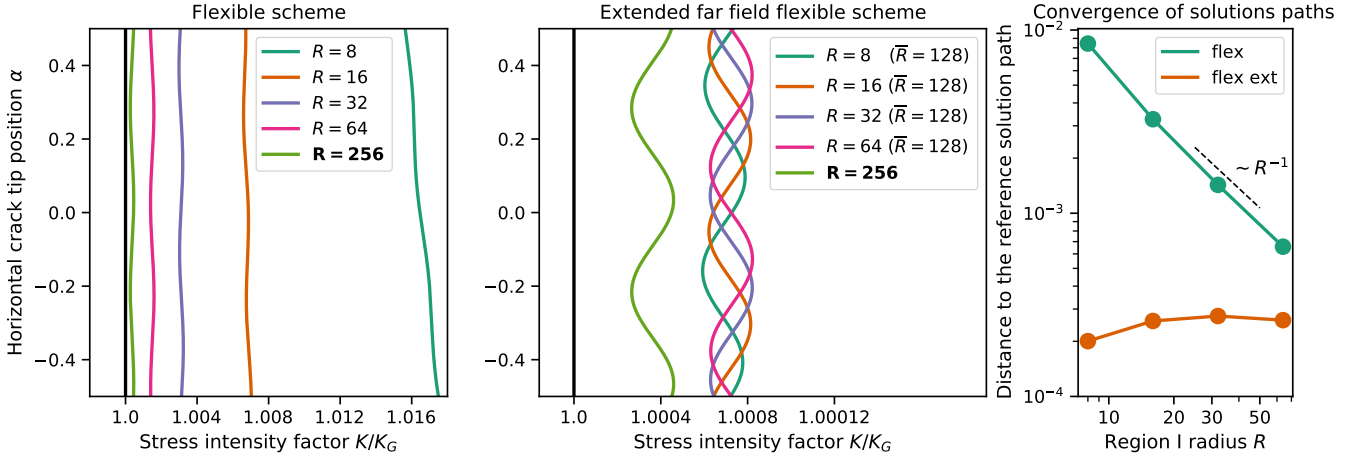


FIG. 7. Solution paths and error analysis for flexible and extended far field flexible boundary schemes. The solution path computed with the flexible boundary scheme with  $R = 256$  serving as a reference in the error analysis.

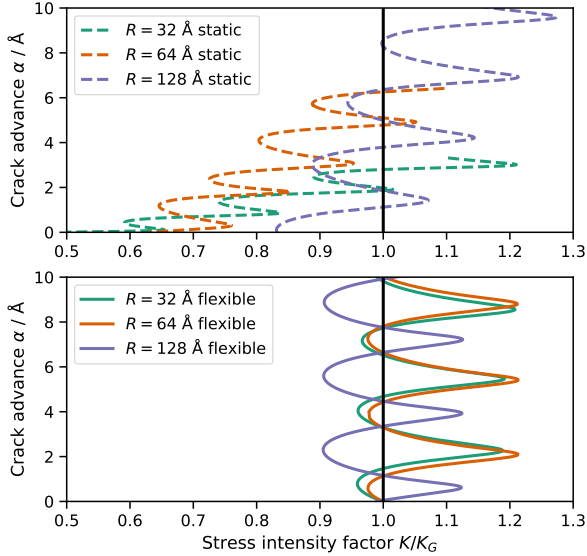


FIG. 8. Comparison of solution paths obtained with Algorithm 3 for a Si(111)[112] crack modelled with the screened Kumagai potential using flexible (solid lines) and static (dashed lines) boundary conditions, for three choices of domain size. For the static cases  $\alpha$  and  $K$  are obtained by a post-processing fit to the CLE solution.

### 1. Pseudo-arclength continuation with the Static and Flexible Boundary Conditions

We first perform arc-length continuation calculations with the Kumagai potential for three choices of domain radii, using both static and flexible boundary conditions. The results are shown in Figure 8. For the static cases, we employ the post-processing fit for  $K$  and  $\alpha$  given in (21), leading to the results shown with dashed lines in the figure. For small domain sizes,

the static solutions are highly tilted, while the flexible solutions show the correct periodic behaviour even at the smallest domain size. We note that the absolute value of  $\alpha$  is somewhat arbitrary, since shifts of the solution path along the crack propagation direction can be incorporated in different choices of the corrector field  $U$ .

The high accuracy of the flexible scheme allows a careful comparison of the lattice trapping predicted by different choices of interatomic potential to be made, as shown in Figure 9. At a domain size of 128 Å the solution paths are already very close to periodic in the crack propagation direction. The energy differences computed with (3) illustrated in the lower panels confirm that there is a critical stress intensity factor  $K_c$  for which the total energy of the atomistic plus continuum system is equal at all stable energy minima, i.e. before and after crack advance. While the range of lattice trapping  $K_- < K < K_+$  predicted by the two potentials is similar, for both potentials  $K_c$  is less than the Griffith equilibrium value  $K_G$ . The values of  $K_G$  used here were computed from the relaxed (111) surface energy, indicating, as well as remaining finite size effects, some of the difference could be attributed to local modifications of the surface energy close the crack tip — a discrepancy that could be further exacerbated by the presence of more complex surface features such as the Pandey  $2 \times 1$  reconstruction.

The unstable part of the screened Tersoff solution path contains an interesting additional feature around  $K = 0.95K_G$ . The inset schematics illustrate how this feature arises: moving along the stable path from (A) to (B), the bond at the crack tip remains intact as the centre of the continuum field  $\alpha$  advances. The bond gradually opens as we move towards point (C) in the unstable part of the solution path, while between (C) and (D) it opens more rapidly as the atoms ‘snap’ apart. We postulate that this sharp feature is associated with the finite cutoff of the potential, which, despite the screening terms that make fracture simulations feasible, is still a modelling assumption. In future work we aim to compute solution paths with DFT to remove the uncertainty associated with the use of simpli-

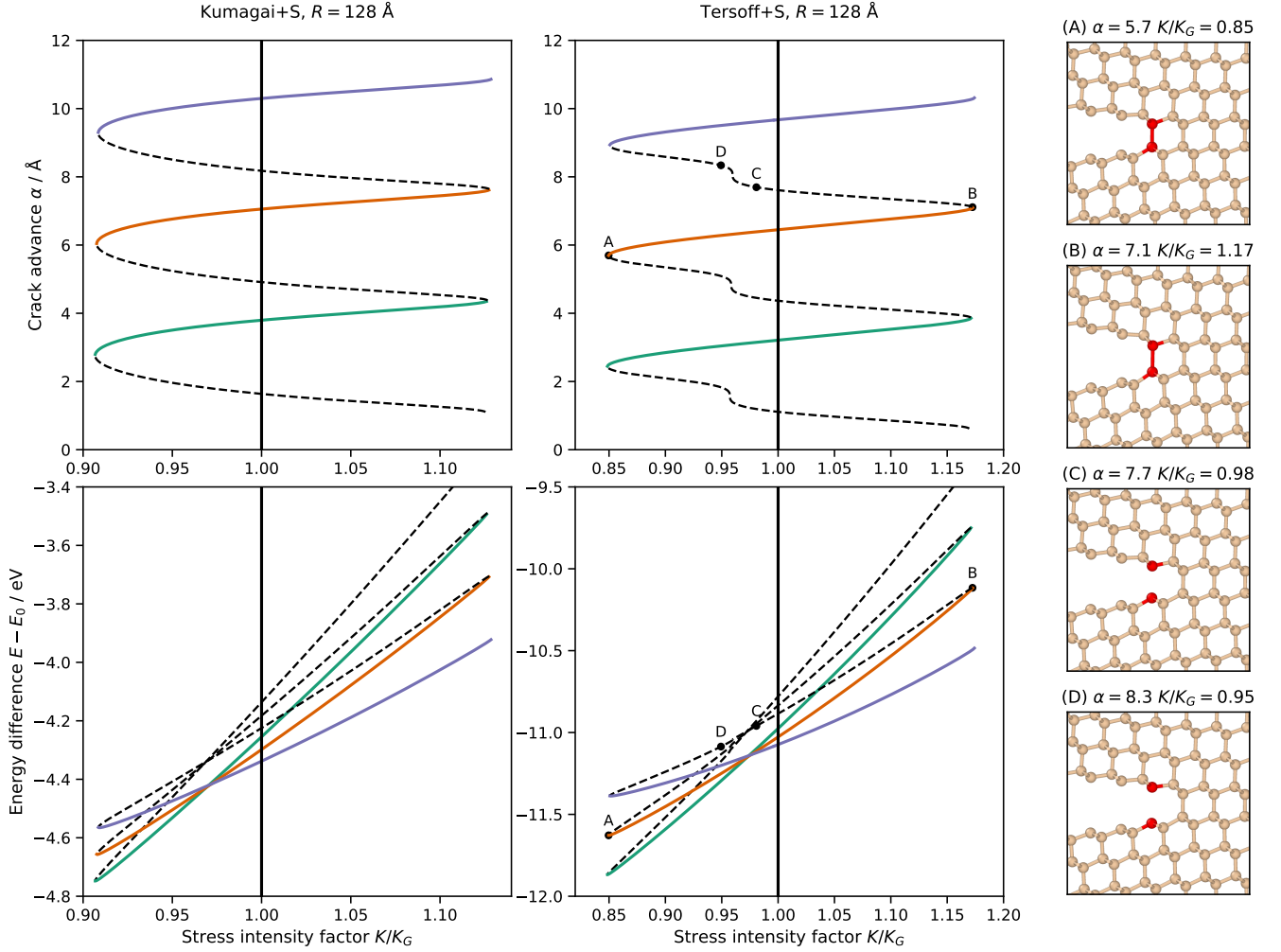


FIG. 9. Comparison of lattice trapping of Si(111)[112] cracks predicted by the screened Kumagai (left panels) and Tersoff (middle and right panels) potentials. Upper panels: solution paths obtained with Algorithm 3, including stable parts (solid lines) corresponding to energy minima and unstable parts (dashed lines) corresponding to saddle points. Lower panels: energy difference with respect to the CLE solution with  $\alpha = 0, K = K_G$ . Right insets: near-tip atomic positions corresponding to marked points A, B, C, D on the Tersoff solution and energy paths, with the opening bond highlighted in red.

fied potentials: this remains out of reach for the present since, despite the considerable improvements in accuracy afforded by the flexible scheme, converged solution paths still require a large number of force evaluations on systems comprising several thousand atoms.

## 2. Predicting the admissible range of $K$

The admissible range of  $K$  is now predicted by finding roots of equation (12), i.e. where  $f_{\alpha}^0(K, \alpha) = 0$ , leading to the predictions shown with the dashed lines in Figure 10. Here,  $K$  is found numerically for each value of  $\alpha$  in a 200-element grid.

For both potentials, the admissible range of  $K$  is in reasonable agreement with that computed in the full solution paths, suggesting that our approach provides a useful way to estimate the stable range of  $K$  for the cost of a fixed number of

force evaluations on the full domain.

## 3. Pseudo-arclength continuation with an extended far-field region

To conclude the numerical tests, we also apply the extended far-field scheme of (14) to the Si(111)[112] crack system, modelled using the screened Tersoff potential. The overall domain size is fixed at  $\bar{R} = 128$  Å, and two choices of radii for Region I are considered:  $R_I = 14$  Å and  $R_I = 46$  Å, chosen since these lead to problems with the same numbers of degrees of freedom as the  $R = 32$  Å and  $R = 64$  Å flexible models considered earlier.

The results are illustrated in Figure 11. Although there is an improvement over the standard flexible scheme in convergence towards the reference  $R = 128$  Å solution path, particularly for the smallest Region I size, these results do not

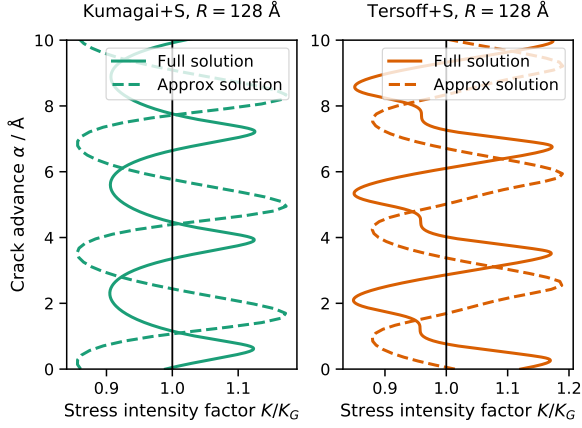


FIG. 10. Comparison of full solution paths obtained by arc-length continuation with Algorithm 3 (solid lines) and corresponding approximate solution paths for  $f_\alpha^0 = 0$  (dashed lines) for a Si(111)[112] crack modelled with the screened Kumagai and Tersoff potentials, using a domain radius of 128 Å.

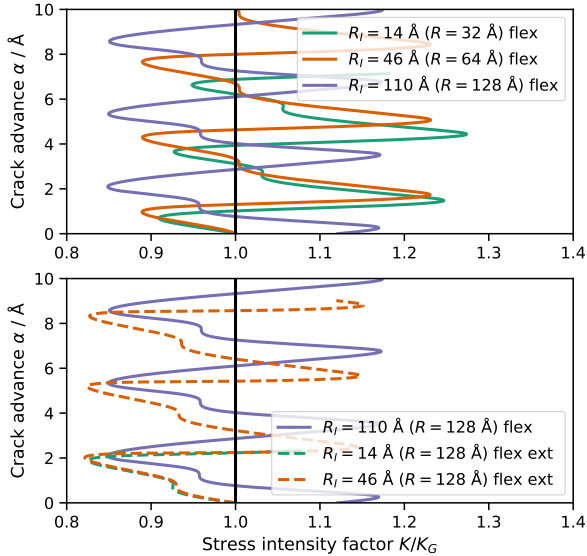


FIG. 11. Comparison of original (denoted ‘flex’, upper panel, solid lines) and extended far field (denoted ‘flex ext’, lower panel, dashed lines) variants of the flexible boundary condition approaches to pseudo-arclength continuation in an Si(111)[112] crack system modelled with the screened Tersoff potential. The  $R = 128$  Å ‘flex’ result is shown in both panels to allow comparison. Calculations with the extended scheme show improved accuracy at smaller domain radii.

provide convincing evidence that a larger far-field region significantly enhances the accuracy of the scheme. This in contrast to the results obtained with the toy model, suggesting that an enhanced CLE predictor that improves the match with the atomistic model is needed to further increase accuracy.

## IV. CONCLUSIONS

In this work we have reported an extension of Sinclair’s flexible boundary condition algorithm to allow full solution paths for cracks to be computed using pseudo-arclength continuation. We have also introduced an extension of the FBC algorithm which allows information to be incorporated from a larger far-field region, and which also provides a stepping stone towards putting the method on a more rigorous mathematical footing. We demonstrated the approach for Mode III fracture with a 2D toy model, and for Mode I fracture of silicon using realistic interatomic potentials that give a qualitatively correct description of fracture.

In future, our approach will enable a detailed study of lattice trapping barriers to brittle fracture to be carried out using increasingly realistic models of interatomic bonding, going beyond the screened bond-order potentials demonstrated here, for example by using machine-learning interatomic potentials [36] or DFT directly. This could help to resolve questions such as the role of blunt-sharp-blunt crack tip reconstruction observed during fracture in the Si(110)[110] crack system [37], where NEB calculations demonstrated the crack is blunted at stable minima and sharp at the unstable transition states. Moreover, the new approach could be expanded to study crack path selection, known to exhibit complex phenomenon in anisotropic materials [38], or the dynamics of three dimensional crack fronts, going beyond previous work that was limited to simple interatomic potentials and small model systems [10]. Truly accurate predictions of critical stress intensity factors and lattice trapping ranges require a quantum mechanical approach, at least near the crack tip. Hybrid schemes such as QM/MM (quantum mechanics/molecular mechanics), previously applied to dynamic fracture [12], could be combined with the algorithms introduced here to make quantitative fracture toughness calculations accurate and affordable. Established routes could then be followed to produce atomistically informed continuum models [39–41].

Before this can be done, however, further work is needed to assess finite-size effects. For the silicon fracture application, we have demonstrated that the flexible scheme is superior to static boundaries, but not yet quantified the convergence rate, meaning that the new algorithms cannot yet be used for predictive materials science. Ultimately, it is hoped that the flexible boundary scheme and numerical continuation techniques can be combined with higher-order far-field predictions to increase accuracy in a quantifiable manner.

Finally, we note that the pseudo-arclength continuation used here would also be applicable to other defects such as dislocations by replacing the stress intensity factor  $K$  as a bifurcation parameter with the applied shear stress, which also enters as a prefactor in front of the CLE solution.

## ACKNOWLEDGMENTS

We thank Christoph Ortner and Lars Pastewka for useful discussions. We acknowledge funding from the EP-

SRC under grant numbers EP/R012474/1, EP/R043612/1 and EP/S028870/1. Additional support was provided by the Leverhulme Trust under grant RPG-2017-191 and the Royal Society under grant number RG160691. The authors would like to acknowledge the University of Warwick Scientific Computing Research Technology Platform for assistance in the research described in this paper.

### Appendix: Computation of tangents in the pseudo-arclength continuation scheme

In the static boundary scheme given by  $F_1 = 0$ , differentiating both sides with respect  $s$  yields

$$\mathbf{0} = H_{s_1} \dot{U}_{s_1} + \dot{K}_{s_1} \mathbf{b}_{s_1}^K, \quad (\text{A.1})$$

where

$$(H_{s_1} \dot{U}_{s_1})(i) = \sum_{j=1}^{N_1} H_{s_1}(i, j) \cdot \dot{U}_{s_1}(j). \quad (\text{A.2})$$

Here  $H_{s_1}(i, j)$  is  $(i, j)$ -th entry of the Hessian operator evaluated at  $s_1$ . In an infinite crystal, the Hessian evaluated at  $s_n$  is an infinite block matrix with

$$H_{s_n}(i, j) = \frac{\partial^2 E}{\partial \mathbf{x}_{s_n}(i) \partial \mathbf{x}_{s_n}(j)},$$

with a short-hand notation  $H_{s_n}$  used to denote its part related to atoms in Region I, which is thus a  $N_1 \times N_1$  block matrix.

The other term on the right-hand side of (A.1) is given by

$$\mathbf{b}_{s_1}^K(i) = \sum_{j=1}^{N_2} H_{s_1}(i, j) \cdot U_{\text{CLE}}^{\alpha_{s_1}}(j),$$

where crucially the summation here is over both the core and the interface regions (thus the Hessian operator here is effectively a rectangular block matrix of size  $N_2 \times N_1$ ), whereas in (A.2) the summation is only over the core region.

It follows from (17) (with  $\dot{\alpha} \equiv 0$  in the static boundary scheme) and (A.1) that

$$\dot{U}_{s_1} = -\dot{K}_{s_1} (H_{s_1}^{-1} \mathbf{b}_{s_1}^K), \quad \dot{K}_{s_1} = \pm (|H_{s_1}^{-1} \mathbf{b}_{s_1}^K|^2 + 1)^{-1/2}, \quad (\text{A.3})$$

provided the square block matrix  $H_{s_1}$  is invertible. The case when it is not invertible is known as a bifurcation point and it will be discussed below.

In the flexible boundary scheme given by  $F_1 = 0$  differentiating with respect to  $s$  implies

$$\begin{cases} \mathbf{0} &= H_{s_1} \dot{U}_{s_1} + \dot{K}_{s_1} \mathbf{b}_{s_1}^K + \dot{\alpha}_{s_1} \mathbf{b}_{s_1}^\alpha \\ \mathbf{0} &= \mathbf{b}_{s_1}^\alpha \cdot \dot{U}_{s_1} + \dot{K}_{s_1} C_{s_1}^{\alpha, K} + \dot{\alpha}_{s_1} C_{s_1}^{\alpha, \alpha}, \end{cases} \quad (\text{A.4})$$

where

$$\begin{aligned} \mathbf{b}_{s_1}^\alpha(i) &= \sum_{j=1}^{N_2} H_{s_1}(i, j) \cdot K V_{\alpha_{s_1}}(j), \\ C_{s_1}^{\alpha, K} &= \sum_{i=1}^{N_2} \left( \mathbf{b}_{s_1}^K(i) \cdot K V_{\alpha_{s_1}}(i) + f(i) \cdot V_{\alpha_{s_1}}(i) \right), \\ C_{s_1}^{\alpha, \alpha} &= \sum_{i=1}^{N_2} \left( \mathbf{b}_{s_1}^\alpha(i) \cdot K V_{\alpha_{s_1}}(i) + f(i) \cdot K V_{\alpha_{s_1}}^{(2)}(i) \right), \end{aligned}$$

with  $V_\alpha^{(2)} = -\partial_1 V_\alpha$ .

Note that (A.4) applies to the newly formulated scheme  $F_2 = 0$  as well, except that the sums defining  $\mathbf{b}_{s_1}^K(i)$ ,  $\mathbf{b}_{s_1}^\alpha(i)$ ,  $C_{s_1}^{\alpha, K}$  and  $C_{s_1}^{\alpha, \alpha}$  should be over  $i = 1, \dots, N_3$ .

If  $H_{s_1}$  is invertible, then equations (17) and (A.4) together imply that

$$\dot{K}_{s_1} = \pm \left( |A_3|^2 + \frac{A_2}{A_1} + 1 \right)^{-1/2}, \quad \dot{U}_{s_1} = \dot{K}_{s_1} A_3, \quad \dot{\alpha}_{s_1} = \dot{K}_{s_1} \frac{A_2}{A_1}, \quad (\text{A.5})$$

where

$$\begin{aligned} A_1 &= \sum_{i=1}^{N_2} - (H_{s_1}^{-1} \mathbf{b}_{s_1}^\alpha(i)) \cdot \mathbf{b}_{s_1}^\alpha(i) + C_{s_1}^{\alpha, \alpha}, \\ A_2 &= \sum_{i=1}^{N_2} (H_{s_1}^{-1} \mathbf{b}_{s_1}^K(i)) \cdot \mathbf{b}_{s_1}^\alpha(i) - C_{s_1}^{\alpha, K}, \\ A_3 &= -\frac{A_2}{A_1} H_{s_1}^{-1} \mathbf{b}_{s_1}^\alpha - H_{s_1}^{-1} \mathbf{b}_{s_1}^K. \end{aligned}$$

With  $(K_{s_1}, \{U_{s_1}(i)\}, \alpha_{s_1})$  and  $(\dot{K}_{s_1}, \{\dot{U}_{s_1}(i)\}, \dot{\alpha}_{s_1})$  known, a standard Newton iteration with initial guess

$$(K_{s_1}, \{U_{s_1}(i)\}, \alpha_{s_1}) + \delta s (\dot{K}_{s_1}, \{\dot{U}_{s_1}(i)\}, \dot{\alpha}_{s_1}),$$

is guaranteed to converge to a new solution  $(K_{s_2}, \{U_{s_2}(i)\}, \alpha_{s_2})$  satisfying  $(F_i, f_K) = \mathbf{0}$  provided  $\delta s$  is small enough (see Figure 1 for visual insight behind this).

Furthermore, the  $s$  derivative  $(\dot{K}_{s_2}, \{\dot{U}_{s_2}(i)\}, \dot{\alpha}_{s_2})$  can now be handily computed with an approximate finite-difference-like scheme, given, for  $F_0 = \mathbf{0}$ , by

$$\mathbf{0} = H_{s_1} \dot{U}_{s_2} + \dot{K}_{s_2} \mathbf{b}_{s_1}^K, \quad (\text{A.6a})$$

$$1 = \sum_{i=1}^{N_1} \dot{U}_{s_1}(i) \cdot \dot{U}_{s_2}(i) + \dot{K}_{s_1} \dot{K}_{s_2} \quad (\text{A.6b})$$

and, for  $F_1 = \mathbf{0}$  (and also for  $F_2 = \mathbf{0}$  after adjusting limits of summation), by

$$\mathbf{0} = H_{s_1} \dot{U}_{s_2} + \dot{K}_{s_2} \mathbf{b}_{s_1}^K + \dot{\alpha}_{s_2} \mathbf{b}_{s_1}^\alpha, \quad (\text{A.7a})$$

$$0 = \mathbf{b}_{s_1}^\alpha \cdot \dot{U}_{s_2} + \dot{K}_{s_2} C_{s_1}^{\alpha, K} + \dot{\alpha}_{s_2} C_{s_1}^{\alpha, \alpha}, \quad (\text{A.7b})$$

$$1 = \sum_{i=1}^{N_1} \dot{U}_{s_1}(i) \cdot \dot{U}_{s_2}(i) + \dot{K}_{s_1} \dot{K}_{s_2}, \quad (\text{A.7c})$$

It is a standard assertion of bifurcation theory [42] that the linear systems of equations given by (A.6) or (A.7) remain solvable even at the points where stability change, corresponding to cases when  $H_{s_1}$  is not invertible, thus allowing us to traverse full the full bifurcation diagram.

## REFERENCES

- [1] J. E. Sinclair and B. R. Lawn, *Int. J. Fract. Mech.* **8**, 125 (1972).
- [2] J. E. Sinclair and B. R. Lawn, “An atomistic study of cracks in Diamond-Structure crystals,” (1972).
- [3] J. E. Sinclair, *Philos. Mag.* **31**, 647 (1975).
- [4] E. Bitzek, J. R. Kermode, and P. Gumbsch, *Int. J. Fract.* **191**, 13 (2015).
- [5] M. Marder, *Int. J. Fract.* **196**, 169 (2016).
- [6] R. Thomson, C. Hsieh, and V. Rana, *J. Appl. Phys.* **42**, 3154 (1971).
- [7] R. Perez and P. Gumbsch, *Phys. Rev. Lett.* **84**, 5347 (2000).
- [8] P. Gumbsch and R. M. Cannon, *MRS Bull.* **25**, 15 (2000).
- [9] L. I. Slepian, *Soviet Physics - Doklady* **26**, 538 (1981).
- [10] J. R. Kermode, A. Gleizer, G. Kovel, L. Pastewka, G. Csányi, D. Sherman, and A. De Vita, *Phys. Rev. Lett.* **115**, 135501 (2015).
- [11] D. Holland and M. P. Marder, “Erratum: Ideal brittle fracture of silicon studied with molecular dynamics [phys. rev. lett. 80, 746 (1998)],” (1998).
- [12] J. R. Kermode, T. Albaret, D. Sherman, N. Bernstein, P. Gumbsch, M. C. Payne, G. Csányi, and A. De Vita, *Nature* **455**, 1224 (2008).
- [13] X. Li, *The European Physical Journal B* **86**, 258 (2013).
- [14] X. Li, *Journal of Applied Physics* **116**, 164314 (2014).
- [15] M. Buze, T. Hudson, and C. Ortner, *ESAIM: Mathematical Modelling and Numerical Analysis* **54**, 1821 (2020).
- [16] J. E. Sinclair, P. C. Gehlen, R. G. Hoagland, and J. P. Hirth, *J. Appl. Phys.* **49**, 3890 (1978).
- [17] J. A. Yasi and D. R. Trinkle, *Phys. Rev. E* **85**, 066706 (2012).
- [18] A. M. Z. Tan and D. R. Trinkle, *Phys Rev E* **94**, 023308 (2016).
- [19] L. Pastewka, A. Klemen, P. Gumbsch, and M. Moseler, *Phys. Rev. B: Condens. Matter Mater. Phys.* **87**, 205410 (2013).
- [20] M. Ostoj-Starzewski, *Probabilistic engineering mechanics* **21**, 112 (2006).
- [21] V. Ehrlicher, C. Ortner, and A. V. Shapeev, *Arch. Ration. Mech. Anal.* **222**, 1217 (2016).
- [22] M. Buze, T. Hudson, and C. Ortner, *Mathematical Models and Methods in Applied Sciences* **29**, 2469 (2019).
- [23] S. Lang, *Fundamentals of Differential Geometry, Graduate Texts in Mathematics* (New York Springer, 1999).
- [24] W.-J. Beyn, A. Champneys, E. Doedel, W. Govaerts, Y. A. Kuznetsov, and B. Sandstede, in *Handbook of Dynamical Systems III: Towards Applications* (2002).
- [25] R. D. Neidinger, *SIAM review* **52**, 545 (2010).
- [26] S. Makri, C. Ortner, and J. R. Kermode, *J. Chem. Phys.* **150**, 094109 (2019).
- [27] R. T. Rockafellar and R. J.-B. Wets, *Variational analysis* (Springer, 1998).
- [28] J. Tersoff, “New empirical approach for the structure and energy of covalent systems,” (1988).
- [29] T. Kumagai, S. Izumi, S. Hara, and S. Sakai, *Comput. Mater. Sci.* **39**, 457 (2007).
- [30] D. Fernandez-Torre, T. Albaret, and A. De Vita, *Phys. Rev. Lett.* **105**, 185502 (2010).
- [31] G. C. Sih, P. C. Paris, and G. R. Irwin, *Int. J. Fract. Mech.* **1**, 189 (1965).
- [32] A. H. Baker, E. R. Jessup, and T. Manteuffel, *SIAM J. Matrix Anal. Appl.* **26**, 962 (2005).
- [33] D. Packwood, J. Kermode, L. Mones, N. Bernstein, J. Woolley, N. Gould, C. Ortner, and G. Csányi, *J. Chem. Phys.* **144**, 164109 (2016).
- [34] A. H. Larsen, J. J. Mortensen, J. Blomqvist, I. E. Castelli, R. Christensen, M. Dułak, J. Friis, M. N. Groves, B. Hammer, C. Hargus, E. D. Hermes, P. C. Jennings, P. B. Jensen, J. Kermode, J. R. Kitchin, E. L. Kolsbjerg, J. Kubal, K. Kaasbjerg, S. Lysgaard, J. B. Maronsson, T. Maxson, T. Olsen, L. Pastewka, A. Peterson, C. Rostgaard, J. Schiøtz, O. Schütt, M. Strange, K. S. Thygesen, T. Vegge, L. Vilhelmsen, M. Walter, Z. Zeng, and K. W. Jacobsen, *J. Phys. Condens. Matter* **29**, 273002 (2017).
- [35] J. Kermode and L. Pastewka, “matscipy package,” (2020), <https://github.com/libAtoms/matscipy>.
- [36] A. P. Bartók, J. Kermode, N. Bernstein, and G. Csányi, *Phys. Rev. X* **8**, 041048 (2018).
- [37] T. D. Swinburne and J. R. Kermode, *Phys. Rev. B* **96**, 144102 (2017).
- [38] A. Mesgarnejad, C. Pan, R. M. Erb, S. J. Shefelbine, and A. Karma, *Phys Rev E* **102**, 013004 (2020).
- [39] J. J. Möller, A. Prakash, and E. Bitzek, *Modell. Simul. Mater. Sci. Eng.* **21**, 055011 (2013).
- [40] A. M. Tahir, R. Janisch, and A. Hartmaier, *Modell. Simul. Mater. Sci. Eng.* **21**, 075005 (2013).
- [41] J. J. Möller, E. Bitzek, R. Janisch, H. u. Hassan, and A. Hartmaier, *J. Mater. Res.* **33**, 3750 (2018).
- [42] K. A. Cliffe, A. Spence, and S. J. Tavener, *Acta Numerica* **9**, 39–131 (2000).